Journal of Physics D: Applied Physics

PAPER • OPEN ACCESS

Electrical breakdown dynamics in an argon bubble submerged in conductive liquid for nanosecond pulsed discharges

To cite this article: Nicholas L Sponsel *et al* 2023 *J. Phys. D: Appl. Phys.* **56** 505202

OPEN ACCESS
IOP Publishing

Journal of Physics D: Applied Physics

J. Phys. D: Appl. Phys. **56** (2023) 505202 (16pp)

https://doi.org/10.1088/1361-6463/acfb1b

Electrical breakdown dynamics in an argon bubble submerged in conductive liquid for nanosecond pulsed discharges

Nicholas L Sponsel[1], **Sophia Gershman**[2] and **Katharina Stapelmann**[1,*]

[1] Department of Nuclear Engineering, North Carolina State University, Raleigh, NC 27695, United States of America
[2] Princeton Plasma Physics Laboratory, Princeton, NJ 08536, United States of America

E-mail: kstapel@ncsu.edu

Received 6 July 2023, revised 10 September 2023
Accepted for publication 19 September 2023
Published 28 September 2023

Abstract

This study delves into the dynamics of cold atmospheric plasma and their interaction within conductive solutions under the unique conditions of nanosecond pulsed discharges (22 kV peak voltage, 10 ns FWHM, 4.5 kV ns^{-1} rate-of-rise). The research focuses on the electrical response, breakdown, and discharge propagation in an argon bubble, submerged in a NaCl solution of varying conductivity. Full or partial discharges were observed at conductivities of 1.5 $\mu\mathrm{S\,cm}^{-1}$ (deionized water) to 1.6 $\mathrm{mS\,cm}^{-1}$, but no breakdown was observed at 11.0 $\mathrm{mS\,cm}^{-1}$ when reducing the electrode gap. It is demonstrated that at higher conductivity electric breakdown is observed only when the gas bubble comes into direct contact with the electrode and multiple emission nodes were observed at different timescales. These nodes expanded in the central region of the bubble over timescales longer than the initial high-voltage pulse. This work offers a temporal resolution of 2 ns exposure times over the first 30 ns of the initial voltage pulse, and insight into plasma formation over decaying reflected voltage oscillations over 200 ns.

Supplementary material for this article is available online

Keywords: plasma–liquid interactions, bubbles, atmospheric pressure plasma, conductive liquid, imaging, nanosecond pulse

(Some figures may appear in colour only in the online journal)

---

[*] Author to whom any correspondence should be addressed.

1. Introduction

Cold atmospheric plasmas (CAPs) are low-temperature plasmas that can be used in a variety of applications, including chemical processing, material surface modification, and biological treatment. Most experiments on plasma–liquid interactions use deionized water due to the reproducibility of results, but in applications from water treatment to medicine, plasma is in contact with liquids of different conductivity [1–4]. Studying plasma in a conductive solution is important because the presence of a conductive medium can influence the behavior of plasma and the reactions that occur within it. For example, the conductive medium can affect the transport of charged particles [5–7] and gas heating within the plasma [8, 9], as well as the production and reactivity of certain species [10–12]. Bubbles and discharges in bubbles are often introduced to increase the surface area of the gas/liquid interface and, hence, promote the transport of plasma generated species into the liquid solution. Many studies that have utilized bubbles to facilitate plasma/liquid interactions in conductive liquids have focused on measuring reactive species generation or chemical degradation on treatment timescales (seconds—hours) [8, 11–13]. In applications, bubbles usually move through the solution, while in experimental studies, bubbles are usually stationary [9, 14–18]. The 3D ellipsoidal shape of submerged bubbles introduce geometry that can help or hinder the local electric field in and around the bubbles [19, 20].

Deeper insight into the breakdown mechanisms and behavior within bubbles will help advance the design of plasma/liquid generators for a desired application. Imaging on timescales that breakdown occurs sheds light on where and how long reactions interact with the liquid boundary. Gershman & Belkind imaged breakdown in a semi-spherical bubble in conductive gel over a 2–10 kV μs pulse in ns resolution [21]. They demonstrated that plasma formed inside a gas bubble continues to propagate and increases in brightness as the current increases over the applied voltage. This shows the difficulty in comparing breakdown in bubbles given the drastic change in electrical parameters based on the geometry and dielectric properties of the liquid around the electrodes. For longer applied voltage timescales, streamer length can bridge electrodes on the order of milliseconds after vaporization begins [22]. These gas-phase streamers occur quicker through the introduction of preexisting bubbles [23]. Expanding research into nanosecond pulsed plasma helps circumvent the issue of thermalizing the liquid as it is the most non-equilibrium CAP achievable in practical terms. Existing research on the use of ns pulsed plasma for liquid breakdown in bubbles is limited and there are practical issues to gathering multiple images over the short interval of time in which to resolve breakdown initiation. Hamdan *et al* captured and characterized breakdown by placing the excited electrode above a grounded needle feeding argon into the liquid, while operating a ns pulser at 1 Hz [24]. Their setup delivered stochastic results as the size, shape, and position of a bubble in relation to when a pulse was delivered could not be predetermined. Lai *et al* approached the issue of resolving breakdown evolution by approximating a bubble to a 2D experiment [9, 25]. The experiment presented in this manuscript holds a free-floating bubble as a constant, such that the 3D ellipsoidal shape, exact timing with the applied pulse, and control over the camera exposure time are manipulated for a stable boundary condition. Additionally, temperature changes to the water are avoided by using single shot ns pulses.

In DI water the bubble/electrode system can be essentially treated as a capacitive system where the free current portion of total current is orders of magnitude less than the displacement current. Energy transfer depends on the impedance of the system and in turn depends on the frequency of the applied voltage. Once ions are added to the water, energy can be transferred to accelerate ions to a drift velocity proportional to the electric field. In water, ions are solvated, surrounded by a hydration shell of reoriented water molecules bound to the ion by electrostatic interactions dependent on the charge and size of the ion. The hydration shell reduces ion mobility by increasing the effective radius of the solvated ion, dependent on the charge of the ion [26, 27]. This affects charge accumulation and relaxation at the liquid interface, effectively changing the breakdown initiation and plasma lifetime at the interface. Babaeva and Kushner simulated breakdown in positive streamers in bubbles, showing the formation of an axial streamer for increased liquid conductivity [28]. Hamdan *et al* observed breakdown in bubbles with increasing conductivity result in a decrease in the lifetime and probability of plasma [24]. Likewise, an observed reduction in streamer length for increased conductivity for longer pulse lengths was observed for long exposure images for a variety of bubble conditions [12, 29]. However, imaging streamers on a long exposure time does not uncover the evolution of the breakdown and its interaction with the liquid/gas boundary where species are directly transported into the liquid.

This study examines the breakdown evolution of a ns pulsed discharge in a boundary condition controlled bubble. We intend to demonstrate that with increasing conductivity a discernible morphology change in streamer formation is observable across the gas phase of the bubble. It is common that with the increase of conductivity, changes to the pulse shape occur. By utilizing control over bubble position and timing, we aim to maintain as similar a pulse shape as possible between conditions. Temporal resolution of breakdown initiation grants access to detailing where the breakdown starts and how it propagates over time, and how breakdown in a conductive solution differs from DI water.

Overall, the value of nanosecond pulsed plasma in conductive solutions lies in their ability to generate highly reactive plasma environments that can be used to perform a wide range of chemical and physical processes with high efficiency and precision. Understanding these effects can help researchers optimize the use of CAP for a range of applications and improve the efficiency of the reactive species generation and their solvation into the liquid medium. Investigation into the processes of electric breakdown under these conditions are still in progress and previous works have primarily focused on longer pulsed timescales and treatment times.

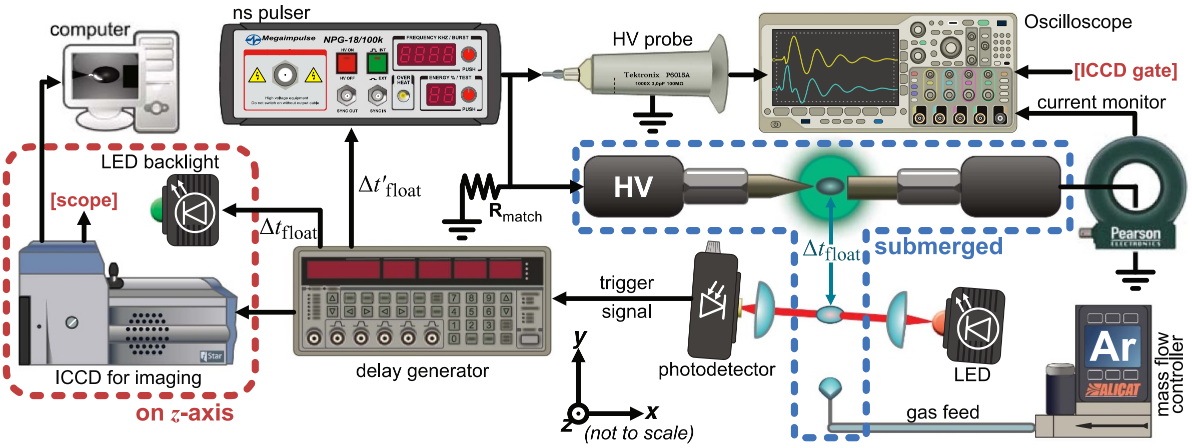

Figure 1. Diagram of experiment in the x–y plane. An argon feed flows bubbles into the bottom of a quartz tank (not illustrated), bubbles float past a pair of emitting and detecting diodes, and traverse between the electrode gap. The triggering signal from the photodetector initiates the delay TTL to activate the backlight LED, ICCD, and pulser. The relevant measurements are recorded by a HV probe, current monitor, and gate width signal from the ICCD. Elements positioned on the z-axis are delineated by the red dotted line. Elements within the blue dotted line are submerged in water within the quartz tank. *Elements not to scale*.

2. Methods

Time-resolved imaging of electric breakdown in bubbles was achieved by using a novel optical triggering design detailed in section 2.1. Section 2.2 explains the analysis of electrical diagnostics for each individual image and how images were selected for comparable breakdown. Details of electric field and current density modeling for the liquid and gas regions of the experiments were summarized in section 2.3.

2.1. Experimental setup

The experimental setup captured free-flowing bubbles between electrodes in synchronization with a high-voltage (HV) nanosecond pulse (Megaimpulse NPG-18/100k). In work preceding this manuscript, it was demonstrated that breakdown initiated at the anode for both positive (excited electrode) and negative (grounded electrode) biased pulses for this experimental setup [30]. For this reason, a positive pulse was used for all cases.

To capture bubbles a stable fluid dynamic regime of rising bubbles was maintained to retain the 3D nature of the shape of a bubble over time [31]. This was to achieve reproducible boundary conditions of the bubbles between subsequent shots. It included a rectangular quartz vessel filled with a NaCl/water solution—varying from a deionized water reference ((1.5 ± 0.4) $\mu\mathrm{S\,cm^{-1}}$), to a 12 mM NaCl solution ((1.6 ± 0.1) $\mathrm{mS\,cm^{-1}}$) and 120 mM NaCl solution ((11.0 ± 0.1) $\mathrm{mS\,cm^{-1}}$). Submerged in the liquid were two tungsten/-copper alloy electrodes positioned horizontally. The excited electrode was mechanically sharpened to a point with a tip radius of $r_{\mathrm{tip}} = (25 \pm 10)\,\mu\mathrm{m}$ while the grounded electrode was polished flat with a cross sectional radius of $r_{\mathrm{electrode}} = (1.64 \pm 0.01)$ mm. A stream of argon gas bubbles came out of a 32 gauge needle below the electrodes controlled with an Alicat MC-series mass flow controller. The argon bubbles detached with an average volume of (1.93 ± 0.22) μl and are the source of the triggering signal for the pulser and imaging systems.

Triggering the applied voltage and the diagnostic instruments at a specific bubble position, at a given time, was achieved by interrupting a collimated beam below the electrode gap. The rising bubble, traveling at 14 $\mathrm{cm\,s^{-1}}$, initiated the pulser, imaging camera (ICCD), and backlight such that the bubble would be positioned within the electrode gap when the voltage pulse was applied (figure 1). The initial trigger signal occurs $\Delta t_{\mathrm{float}}$ before the bubble has reached the desired position between the electrodes ($\Delta t_{\mathrm{float}}$ is the time it takes a bubble to reach the inter-electrode gap). The bubble shape was perturbed when the inter-electrode gap, $1\ \mathrm{mm} < d_{\mathrm{electrode}} < 2$ mm, was set to a distance shorter than the major-axis diameter of the bubble, $D_{\mathrm{bubble}} = (1.72 \pm 0.03)$ mm. The delay generator (SRS DG645 Opt. 5) can time the trigger signals such that the bubble was in a desired position between the electrodes when the voltage pulse reached the electrodes. To achieve accurate timing, the time for internal pulser delay and cable delay were separately compensated for from the ICCD (Andor iStar 734) and electronic diagnostic timing. The voltage was measured with a HV probe (Tektronix P6015A) at the HV electrode terminal, the current was measured after the grounded electrode with an inductive current monitor (Pearson Model 6600). Voltage, current, and gate monitoring signal from the ICCD were recorded by a 5 $\mathrm{GS\,s^{-1}}$ oscilloscope (Rigol DS6104, 1 GHz, 5 $\mathrm{GS\,s^{-1}}$).

Nanosecond time resolution for imaging the discharge initiation and propagation was achieved by varying the ICCD gate delay so that the camera was activated at a desired time during the voltage pulse, always measured from the start of the pulse. Each ICCD frame was taken during a new, single, discharge event and the amplification (MCP) of the ICCD was held constant to accurately compare images. This method of using separate bubbles to gather single-shot nanosecond time steps was subject to slight variations in bubble position. The nanosecond-scale exposure gates used to capture

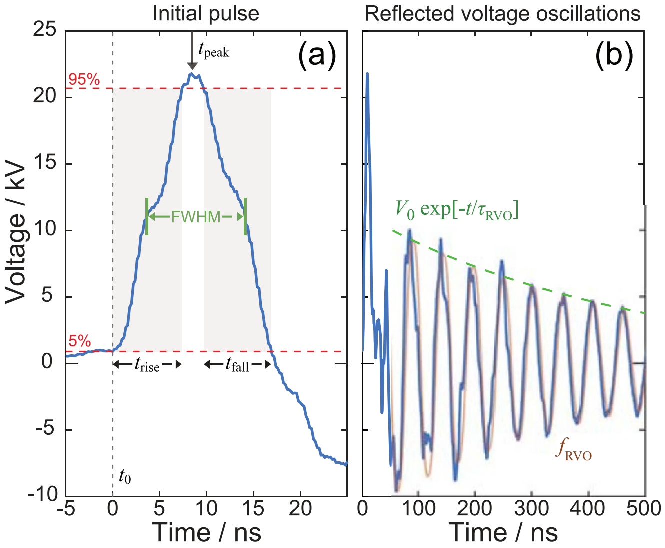

Figure 2. The measured voltage is divided into the (a) initial pulse region and the (b) reflected voltage oscillation (RVO) region. The initial pulse defines the overall timing such that t_0 begins at 5% of peak voltage, V_{peak}. t_{rise} is the time between 5% to 95% of V_{peak}, t_{peak} occurs at V_{peak}, and t_{fall} is the time between 95% to 5% after V_{peak}. The width of the pulse is defined by the full-width half-max. The RVO is defined by the fitted average frequency after the pulse, f_{RVO}, and the decay of the envelope of the RVO by the characteristic time, τ_{RVO}. Overall temporal uncertainty is ±2 ns.

breakdown evolution collect insufficient light from the backlight to delineate the bubble boundary for each shot. Hence, longer exposure times ($\Delta t_{\mathrm{gate}} = 10^{-7} - 10^{-4}$ s) were used throughout the process to monitor shape and position of the bubbles. Most observations showed changes in the horizontal position of bubbles relative to the electrodes and perturbations of bubble shape due to their interaction with the sharp electrode tip as they pass through the gap. Decreasing the inter-electrode gap and perturbing the bubble increased the local electric field resulting in a higher probability of achieving a discharge with each applied pulse. The horizontal position of the bubble centroid varied with an uncertainty of $\pm 50\,\mu$m (see supplementary material figure S1). The equipment used in this experiment could not capture the breakdown from a single discharge event with ns time step resolution. Therefore, 2 ns–50 ns exposures were collected during separate voltage pulses, corresponding to discharge events in different individual bubbles.

2.2. Data analysis

The applied voltage pulse was unmatched and was divided into an initial pulse region (figure 2(a)) and a decaying reflected voltage oscillations (RVOs) region (figure 2(b)). The measured RVO were the effect of not only the decaying reflected pulse across the transmission line, but all of the RLC circuit responses contributed by the cables, electrodes, liquid, and diagnostic equipment in circuit. The beginning of the pulse was defined at 5% of the peak voltage, $t_0 = t|_{V=0.05V_{\mathrm{peak}}}$. The rise (5%–95%) of the applied voltage pulse occurred between 0 ns $< t_{\mathrm{rise}} <$ 7.5 ns, peaked at $t_{\mathrm{peak}} =$ 8.5 ns, and fell between 9.5 ns $< t_{\mathrm{fall}} <$ 16.5 ns (figure 2(a)). For all shots, the initial rate of rise over the first 4 ns was (4.5 ± 0.9) kV ns^{-1} and were unaffected by physical variations between the bubble and electrodes. The initial pulse width at FWHM was measured to be (9.3 ± 2.3) ns. The frequency response of the system characterized by the decaying RVO influenced by the equivalent circuit of the gas/liquid/probe system was approximately $f_{\mathrm{RVO}} \approx 19$ MHz. The characteristic time of the decay was $\tau_{\mathrm{RVO}} \approx 250$ ns, but varied with bubble position and liquid conductivity. In this manuscript t is used to denote points or intervals of time, while τ is used to denote characteristic decay times.

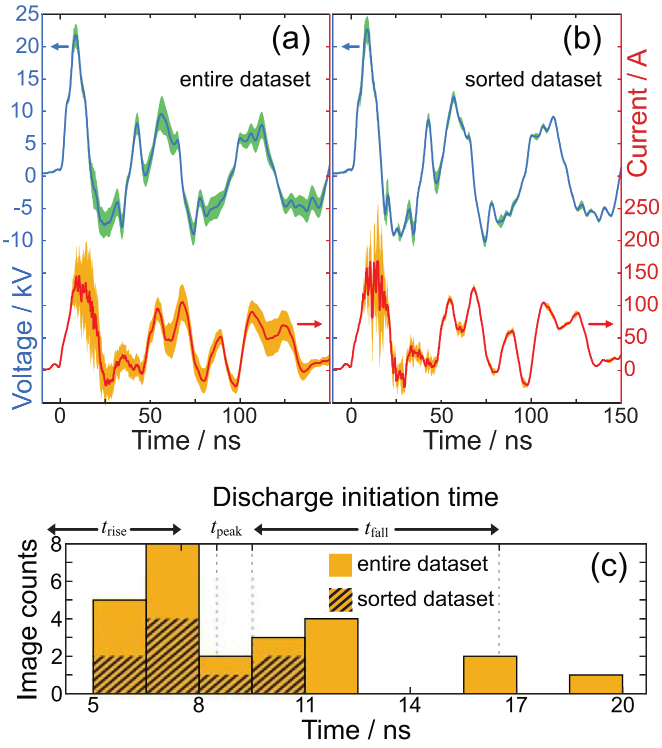

Figure 3. Uncertainty of breakdown is narrowed by comparing voltage and current waveforms for (a) all shots to (b) sorted images. A (c) histogram of discharge initiation time to show statistical variation before sorting data by voltage similarity. After sorting, the late discharge delays on the histogram were filtered out completely and the uncertainty in the voltage and current waveforms were greatly reduced.

The average peak voltage for all images of electric breakdown was $V_{\mathrm{peak}} = (21.96 \pm 1.83)$ kV. The standard deviation in voltage over the RVO region of the waveform increased to ±3.18 kV and stayed consistently above ±2 kV throughout the first 200 ns (figure 3(a)). Variation in voltage and current from one image to another was observed due to differences in spatial features of individual bubbles (e.g. size, deformation, or position with respect to the electrodes) and their corresponding impact on electrical properties of the system. To accurately compare images of similar electrical breakdown characteristics, the voltage waveform of each shot was quantitatively compared to every other shot with a MATLAB script and sorted into groups with similar electrical measurements (see supplementary materials figure S2). The MATLAB script excluded any erratic discharges and assured that only similar discharges are compared, as seen from the reduced uncertainty between traces; they were overall down by 53% and down by 61% for the RVO region. Likewise, the current waveforms between figures 3(a) and (b) showed a reduction in standard deviation between shots after sorting. High frequency electromagnetic noise produced by the individual discharges was used to time the initiation of the discharge. EMI signals were isolated by applying a 100 MHz highpass filter to the current waveform (each signal shown in supplementary material figure S3). Figure 3(c) shows the histogram of discharge initiation time for both the entire dataset and sorted dataset, and their relation to the pulse rise and fall. The sorting algorithm helped compare images with similar electrical stimulation at any timestep as well as exclude images for which discharge began much later.

On average the breakdown began between the half-max of the rising edge and the peak of the pulse in the sorted dataset. Three discharge conditions were observed across the entire dataset:

- Full discharge, where emission was observed near both electrodes by the end of the initial pulse,
- Partial discharge, where emission was only observed near the sharp electrode for the entirety of RVO, and
- No discharge, where no emissions or EMI were detected.

The sorted dataset, used to compare emissions, only included images and electrical data for the full discharge case. Although data sorting significantly limited the number of images analyzed simultaneously, it was necessary to ensure that discharge conditions were as similar as possible between single-shot events of different bubbles when comparing emission behavior over time.

2.3. Field modeling

Ansys Maxwell was used to approximate the electric field strengths and current densities at the tip of the electrode, at the surface boundary between the liquid and gas, and within the gas region of the bubble for various bubble shapes and positions relative to the electrodes (figure 4). This was done to determine if the E-field strengths in water were high enough to induce electrostrictive cavitation at the electrode, to assess whether Ohmic heating in the water was significant enough for vaporization, and to estimate breakdown thresholds within the gas region of the bubble.

Electric fields, calculated at the boundary between the bubble and the liquid, were collected and averaged across circumferential rings mapped around the bubble. The magnitude of current density, likewise, was calculated and averaged at these rings (see supplementary material figure S4). Each bubble geometry was calculated for each conductivity for the experiment. The calculated E-field in the 3D model was used to determine a proportionality constant, K_{bubble}, to approximate the E-field near the surface of the bubble using the applied voltage,

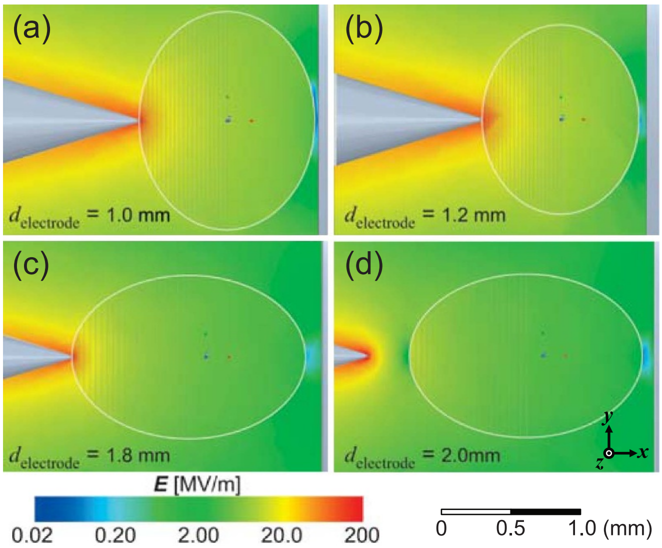

Figure 4. Ansys Maxwell 3D simulations for varying electrode gap distances and bubble dimensions associated with the images captured experimentally for a liquid conductivity of $\sigma = 1.6\ \mathrm{mS\,cm^{-1}}$ and electrode tip radius of $r_{\mathrm{tip}} = 25\ \mu\mathrm{m}$. Perturbed bubbles are modeled with a reduced diameter of (a) $D_{\mathrm{bubble}} = 0.97$ mm and (b) $D_{\mathrm{bubble}} = 1.14$ mm. The free-floating bubbles (c) and (d) assume oblate azimuthal symmetry with a major diameter of $D_{\mathrm{bubble}} = 1.72$ mm. E-fields within the gas region of the Ar bubble remain at or above the 2 $\mathrm{MV\,m^{-1}}$ breakdown threshold.

$$E_{\mathrm{bubble}}\left(t\right) \approx K_{\mathrm{bubble}} V_{\mathrm{pulse}}\left(t\right)\ , \tag{1}$$

such that,

$$K_{\mathrm{bubble}} = \left\langle \frac{\left|\mathbf{E}_{\mathrm{ring}}\right|\left(t\right)}{V_{\mathrm{pulse}}\left(t\right)} \right\rangle\ , \tag{2}$$

where $|\mathbf{E}_{\mathrm{ring}}|(t)$ is the magnitude of the E-field plotted by Ansys across a given 1-dimensional ring. The voltage waveform used for field modeling was the superposition of Gaussian functions fitted to the average measured voltage waveform,

$$V_{\mathrm{pulse}}\left(t\right) = \sum_i a_i \exp\left[-\left(\frac{t-b_i}{c_i}\right)^2\right]\ , \tag{3}$$

where the values for the coefficients are collected in table 1 in units of kV and ns.

The slight variations in bubble shape, as well as electrode position, required investigation into the change of electric field and current density around the gas boundary of the bubble. Calculations show a greater change in direction of $\mathbf{E}$ and $\mathbf{J}$ around the bubble when the bubble was closer to the sharp electrode. This was due to the bubble shape being compressing along the x-axis as the bubble passes between the electrodes (figures 4(a) and (b)). The local E-field enhancements

Table 1. Values for coefficients of $V_{\text{pulse}}(t)$ (equation (3)) acquired to fit the measured pulse shape. The analytical function, $V_{\text{pulse}}(t)$, is used in the Ansys Maxwell transient solver, and to solve the free and displacement current densities in Mathematica.

i	a (kV)	b (ns)	c (ns)
1	17.53	8.142	4.039
2	11.68	14.60	3.755
3	5.988	3.268	1.519
4	3.668	19.51	2.230
5	0.555	–0.738	7.972

for a free-floating bubble (figures 4(c) and (d)) resulted in a reduction near the apex of the bubble when the major-axis diameter of the bubble was parallel with the x-axis. The field reduction intensified when the liquid layer between the sharp electrode and the bubble's apex thickened, as observed with the 270 μm layer in figure 4(d). The real perturbed bubble shapes are not modeled because in the 2D images the bubble cross-section obscures the bubble curvature around the electrode. Instead perturbed bubbles were modeled as ellipsoids with a reduced diameter along the gap direction. In general, the E-field at the boundary interface decreases with increased inter-electrode gap distance. However, there was a calculated drop in the E-field for the smallest gap distance along the x-axis such that the bubble was elongated along the y-z plane. The change in the bubble surface area reduced the liquid layer at the ground and slightly changing local E-field enhancements as the bubble eccentricity was altered. In all cases, the local E-field within the liquid region was reduced on the ground-side of the bubble. Overall, the change between figures 4(a) and (b) was small and within the error propagated between fitting values for K_{bubble} and averaging across the path of the 1-D rings that encompassed the bubble surface in Ansys.

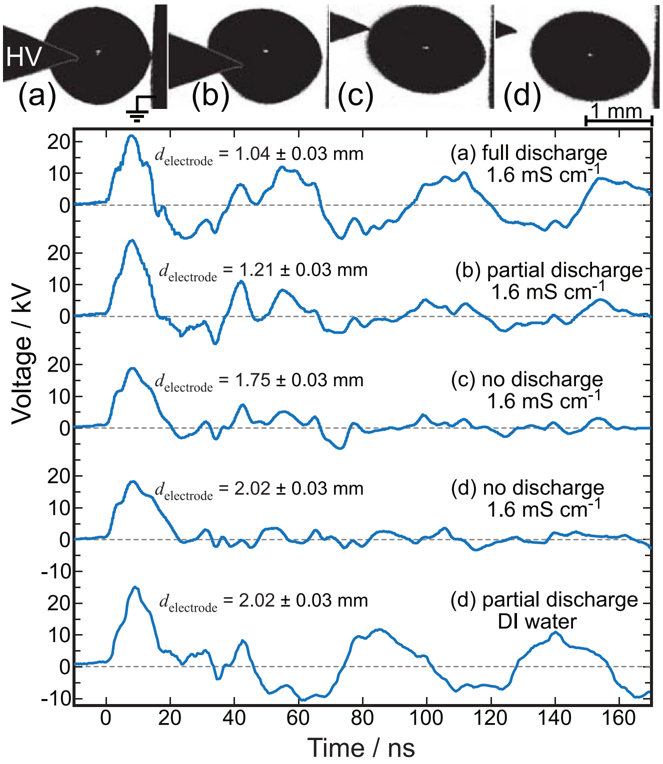

Figure 5. Voltage waveforms and images captured for various bubble dimensions and electrode gap distances for a liquid conductivity of $\sigma = 1.6$ mS cm^{-1} and $\sigma = 1.5$ μS cm^{-1} ((d) only). For NaCl solution of 1.6 mS cm^{-1}, discharge was achieved in perturbed bubbles (a) and (b), but not in free-flowing bubbles (c) and (d). RVO became increasingly enhanced with reduced water layer between the bubble and electrode. For DI water, breakdown is achievable for free-flowing bubbles (d) and it is accompanied by high amplitude RVO. The radius of curvature of the electrode tip is $r_{\text{tip}} = (25 \pm 10)$ μm, and bubble diameters, D_{bubble}, are (a) (1.75 ± 0.15) mm, (b) (1.63 ± 0.05) mm, and (c) and (d) (1.73 ± 0.03) mm.

3. Results

Observations for the electrical response, breakdown, and propagation behavior in an argon bubble in NaCl solution are presented for time resolved imaging. Section 3.1 documents the changes in the electrical signals observed after ions were introduced to the water. Section 3.2 revisits discharge in DI water and reports on charge accumulation at the liquid/gas interface of the bubble for the formation of surface ionization waves. Section 3.3 presents high temporal resolution imaging of the breakdown over the initial pulse of the applied voltage. Observations of the discharge during the RVO time interval of the applied voltage are presented in section 3.4. During the RVO time, the dominant central emission node that formed during the initial pulse grows quasi-isotropically as the RVO decays.

3.1. Electrical response in the case of conductive solutions

For DI water, >700 images were collected showing breakdown occurring in both liquid and gas regions between the inter-electrode gap. After NaCl was added to the water, optical emission was observed for only the gas region of the bubble for a liquid conductivity of $\sigma = 1.6$ mS cm^{-1} (360 images). Increasing the conductivity to $\sigma = 11.0$ mS cm^{-1} resulted in no observations of breakdown (50 images). For the NaCl solution the E-field in the gas phase was increased by allowing the bubble to come in contact with the electrode. The resulting increase in E-field was sufficient to achieve breakdown in solutions of 1.6 mS cm^{-1}. Therefore, all the images presented here correspond to the conditions of a disturbed bubble and conductivity of 1.6 mS cm^{-1} (figure 5(a)).

The perturbed and free-flowing bubble boundaries in figure 5 were similar to those represented in the E-field models in figure 4. Even with the attempts to have a matching load, the RVO changed considerably. RVO were reduced for increasing inter-electrode distance or increasing thickness of the liquid layer and diminish when no discharge was present. The electrical characteristics were also different for the two perturbed bubble positions (figures 4(a), (b) and 5(a), (b)). In both situations, the bubble was in contact with the sharp electrode but the liquid layer between the gas bubble and the flat grounded electrode changed in thickness. When the liquid layer on the grounded side was (36 ± 12) μm, the breakdown probability was $(86 \pm 11)\%$, but when the thickness was (62 ± 14) μm the probability decreased to $(20 \pm 13)\%$, where the standard error of the proportion was calculated as $\mathrm{SE} = \sqrt{p(1-p)/n}$, for successful events (p) of a sample size of single shots (n).

The greater RVO observed in the high breakdown probability case suggest that HV electrical stimulation was prolonged over a longer period of time in a manner that approximates a decaying AC wave. The RVO region decays for hundreds of ns after the initial pulse and the time of τ_{RVO} varied depending on the magnitude of the breakdown. In DI water the RVO decayed slowly over 450 ns for a low intensity discharge, or as quickly as 150 ns for a high intensity discharge for breakdown in the liquid region before the bubble is reached.

In addition, RVO reached $V \approx 10$ kV in the case of higher probability of discharge, $V_{\mathrm{RVO}} \approx 5$ kV for lower probability case, and $V_{\mathrm{RVO}} \approx 2$ kV for free-flowing bubbles where $D_{\mathrm{bubble}} < d_{\mathrm{electrode}}$. The standard deviation of the voltage measurement for the RVO region of bubble (d) is approximated as $V_{\mathrm{RMS}} = 1.1$ kV, or 6% of the peak voltage. Under these conditions the voltage waveform for bubble (d) in DI water approximated that of bubble (a) for conductivity of 1.6 mS cm^{-1}, with average voltages calculated over τ_{RVO} at $V_{\mathrm{RMS,\,DI}}|_{(\mathrm{d})} = 5.0$ kV and $V_{\mathrm{RMS,\,1.6\,mS/cm}}|_{(\mathrm{a})} = 5.1$ kV. For NaCl solution of $\sigma = 1.6$ mS cm^{-1} temporal breakdown evolution was compiled for the high probability case of bubble (a).

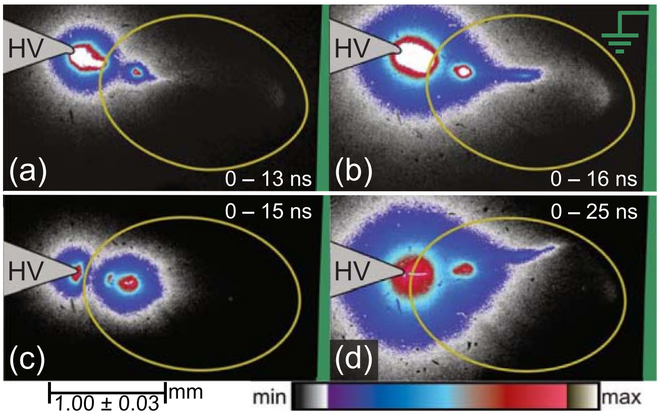

Figure 6. Ionization wave propagation in an Ar gas bubble submerged in deionized water in a pin-to-rod electrode gap with an electrode gap of $d_{\mathrm{electrode}} = (2.02 \pm 0.03)$ mm, bubble diameter $D_{\mathrm{bubble}} = (1.73 \pm 0.03)$ mm, and HV electrode tip radius of $r_{\mathrm{tip}} = (25 \pm 10)$ μm. The ICCD exposure gate starts before the pulse is triggered and ends at (a) 13 ns, (b) 16 ns, (c) 15 ns, and (d) 25 ns. Breakdown in the liquid region takes the form of a streamer from the tip of the sharp electrode to the apex of the bubble. The intensity of the streamers increase with the thickness of the water ((a) and (b) – 270 μm, (c) and (d) – 70 μm), hence with streamer length. In the bubble, the streamer propagation exhibits a curved path across the bubble over time suggesting a surface ionization wave across the liquid/gas phase boundary.

3.2. Streamer propagation in DI water

For the DI water (1.5 μS cm^{-1}) case, the early stages of streamer formation were observed in the gas region of the bubble. The emission detected during breakdown revealed two distinct processes: the conductive channel in the liquid region ($n_e \approx 10^{18} - 10^{19}$ cm^{-3} [32, 33]) and a separate emission feature in the gas region. Two different bubble positions were compared for the same inter-electrode distance of $d_{\mathrm{electrode}} = (2.02 \pm 0.03)$ mm in figure 6. Figures 6(a) and (b) corresponded to the bubble position shown in figure 5(d), while figures 6(c) and (d) were for a bubble floating closer to the sharp electrode for the same $d_{\mathrm{electrode}}$. The ICCD exposure gate was opened prior to the pulse and closed during or after the initial pulse, such that emission intensity for the subsequent time steps are integrated cumulatively. For the first ~10 ns, emission formed at the tip of the electrode before discharge in the gas was observed and was detailed in [30].

Image intensity for figure 6 was offset so that the brightest pixels in the gas region were set to be the overall maximum pixel value at 13 ns. The propagation distance of the emission was gauged from the maximum pixel value up to where the emission reached 10% of that intensity (illustrated by the white/purple boundary on the minimum side of the color scale in figure 6). The distances measured from the peak emission to the 10% value limit in the gas region were as follows: 190 μm for figure 6(a), 620 μm for figure 6(b), 325 μm for figure 6(c), and 900 μm for figure 6(d). When the electrode was ~270 μm away from the apex of the argon bubble (figures 6(a) and (b)), a larger plasma channel formed in the liquid increasing the local E-field—compared to when the argon bubble is ~70 μm away from the electrode (cf figures 6(c) and (d)). The large channel case resulted in an ionization wave speed of ~150 km s^{-1} across the liquid/gas phase boundary, and the small channel case resulted in an ionization wave speed of ~50 km s^{-1}. Emission that was less intense than the 10% threshold (scaled to grayscale) was observed to curve towards the ground-side of the bubble, but full propagation between electrodes was not observed for bright emission after the E-field was diminished by the end of the applied voltage pulse.

3.3. Breakdown behavior in NaCl solution: initial pulse

An exposure time of $\Delta t_{\mathrm{gate}} = 2$ ns was used for imaging the discharge occurring during the initial pulse (figure 7). Yellow lines define the gas bubble boundaries for the entire dataset and illustrate the uncertainty of the bubble positions. To resolve the relative intensity of the emission nodes (bright regions) captured in the ICCD images (figures 7(a)–(e)), the measured intensity was integrated in the vertical direction (figure 8). Though several shots were filtered out using the data sorting method described in section 2.2, a consistent step-through of the initial pulse uncovers the spatial and temporal evolution of the breakdown. The emission initiated at the sharp electrode (figure 7(a)), with an early diffuse glow detectable in the gas region of the bubble during the second half of t_{rise}. For DI water, the initial breakdown occurred at the tip of the

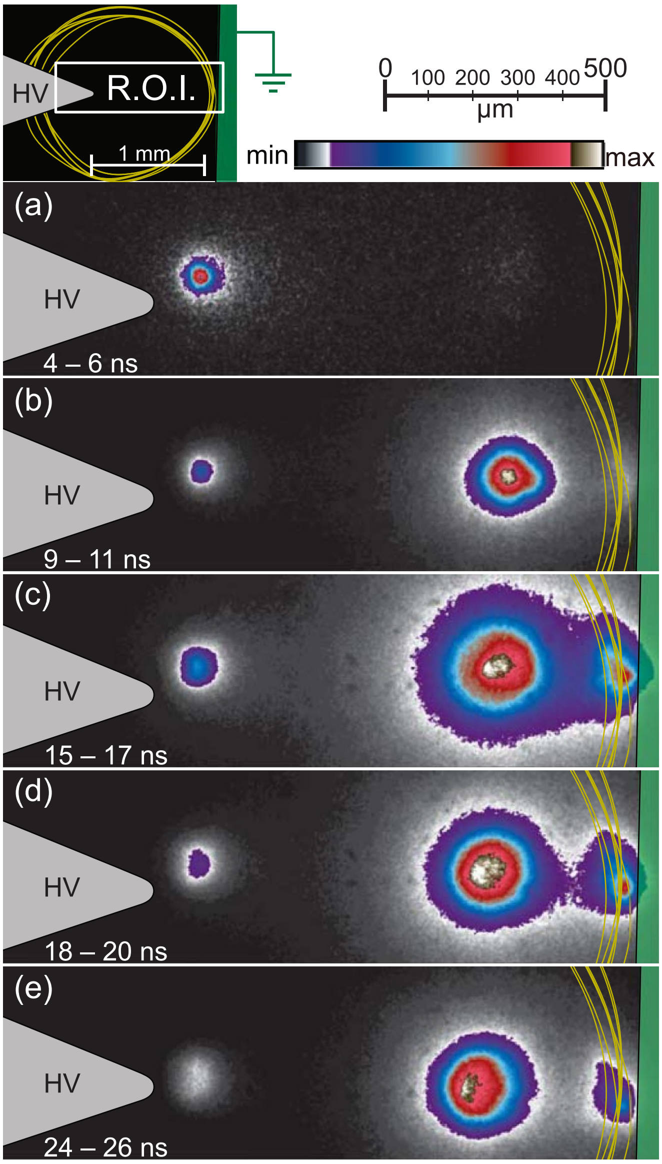

Figure 7. Imaging of breakdown over 4 ns $< t <$ 26 ns with $\Delta t_{\text{gate}} = (2 \pm 2)$ ns. The images presented are zoomed into the region-of-interest (R.O.I.) consisting of the gas region in the bubble between the electrodes. During t_{rise} (a), the corona-like emission node initiates near the tip of the anode. After t_{peak} (b) emission begins in the gas phase at the central node closer to the cathode. During t_{fall} (c) and (d) breakdown at the liquid layer and grounded electrode begins to produce emission. After the pulse (e) emission detected at the electrode-proximate nodes rapidly attenuate, while the central emission node decay remains dominant. Physical parameters: $\sigma = 1.6$ mS cm^{-1}, $d_{\text{electrode}} = 1.04$ mm, $D_{\text{bubble}} = 1.75$ mm.

electrode where E-field enhancements are greatest. For the cases of the perturbed bubbles, the E-field at the bubble interface was on the same order of magnitude as the electrode tip. E-fields calculated using the ANSYS model (section 2.3 and figure 4) declined from 24 MV m^{-1} to 6 MV m^{-1} across the x-axis from the apex of the bubble closest to the sharp electrode tip to the center of the bubble by t_{peak}. The initial corona-like discharge was likely on the gas side of the bubble interface given that the bright spot imaged in figure 7(a) was $\sim$80 μm away from the electrode tip. The central node emission began around t_{peak} and increased in brightness as voltage decreased (figures 7(b) and (c)). Over the course of t_{fall}, emission emerged at the liquid layer between the gas and bubble which is better illustrated in figure 8. The emission at this node was slightly above the detection limit from background emission (color-coded orange) at $\sim$10 ns, but became significantly more pronounced by the next time step (color-coded gold) at $\sim$14 ns. While the central node remained dominant after the measured voltage returned to 0 kV at 17 ns, the nodes close to the electrodes decreased in intensity and broaden as the electrodes change polarity. The overall emission intensity decreased rapidly following the first voltage pulse.

It is important to note that the appearance of multiple emission nodes was dependent on the liquid layer thickness. For example, in the case of the bubble in figure 5(b) only a partial breakdown at the sharp electrode tip was present over the initial pulse (see supplementary material figure S6). In addition, across the entire data set, there were variations in intensity and timing of the emission node that appeared between the bubble and the grounded electrode. After using the sorting algorithm, subsequent images follow a smooth trend of increasing and decreasing intensity in conjunction with the voltage pulse (figure 8); the temporal measurement uncertainty was ±2 ns.

3.4. Breakdown behavior in NaCl solution: broader time period

In this section, we present images taken before, during, and after the first pulse and with different exposure times. The variations in intensity, due to different exposure times and the relative emission intensities between the initial pulse and RVO, were compensated by normalizing the signal. Maximum intensity normalization of the vertically integrated emission values was used to qualitatively compare the broadening of the emission nodes over time (figure 9). This analysis procedure revealed the structure of the emission nodes by avoiding oversaturation.

The earliest image (figure 9(a)) corresponds to a time of <4 ns, which is during the first half of t_{rise}. At this time, the faint and diffuse light resembled a Townsend discharge. As shown by the discharge initiation times in figure 3(c), there were no high-frequency EMI signals before this time, suggesting that a conducting channel had not yet formed. Over the remainder of the initial pulse, several emission nodes, which are more diffuse in nature than those observed in DI water (cf figure 6), developed as detailed in section 3.3. During the entire first pulse, there was no evidence of sharp curved emission resembling streamers as in figure 6 for DI water. All the emission nodes appeared more diffuse for conductive solution than in DI water. After the first period of the RVO, emission at the central node appeared to broaden in comparison to the more narrow peak that persisted throughout figures 7 and 8. The emission that began in the central node expanded relatively isotropically and the intensity of this region was the dominant source of emissions. After 200 ns the overall light detected was more

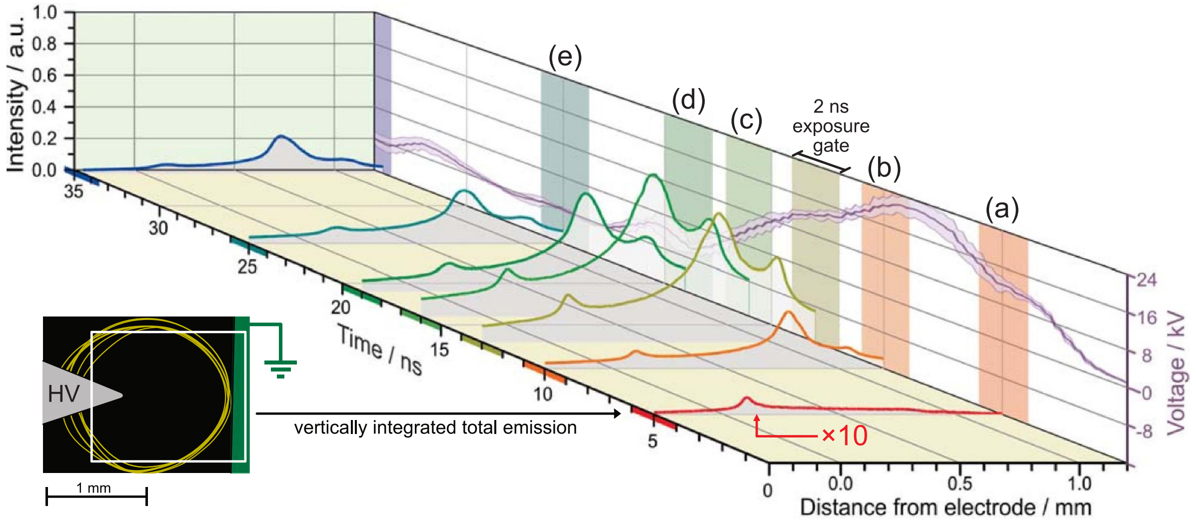

Figure 8. Vertically integrated emission values summed to demonstrate spatial evolution of discharge for figure 7. Δt_{gate} for each shot are overlaid in color against the voltage waveform (z–y plane) and labeled in comparison to figure 7. The signal for (a) has been increased by an order of magnitude for better visualization. The greatest increase of emission occurs after 12 ns on the downslope of the pulse. Once the voltage is negative the electrode-proximate emission nodes decay rapidly while the central emission node remains prominent.

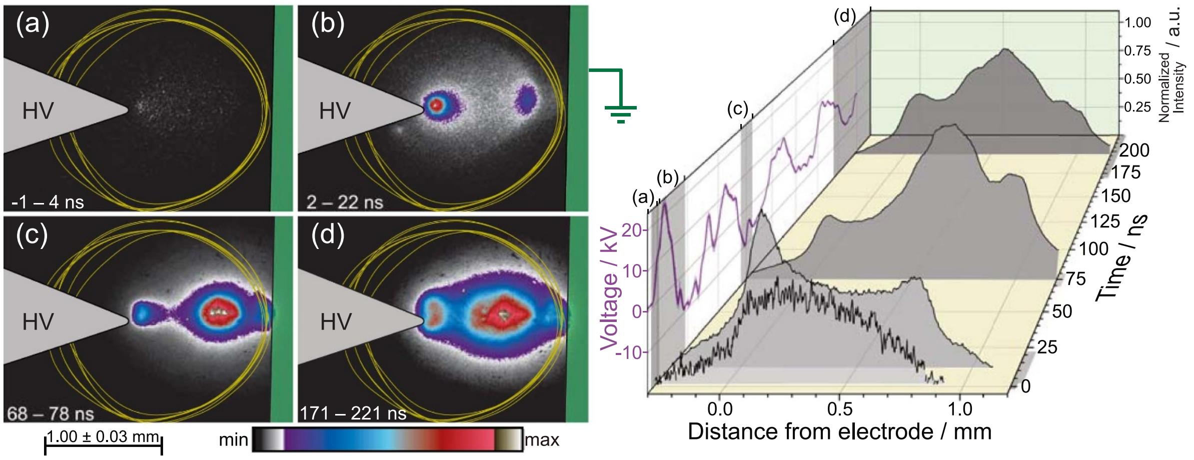

Figure 9. (a) Diffuse discharge across the bubble is observed before t_{peak}, followed by (b) the formation of bright corona-like discharge at the electrode during t_{fall}. (c) Bridging of the emission nodes in the center of the bubble occurs early in the RVO region, and (d) quasi-isotropic expansion of emission in the gas region of the bubble occurs later in the RVO region. Yellow lines delineate bubble boundaries of various shots. Vertically integrated emission values are summed to demonstrate spatial evolution of the discharge. The imaging gate widths are overlaid in gray against the voltage waveform (z–y plane). Physical parameters: $\sigma = 1.6\ \mathrm{mS\,cm^{-1}}$, $d_{\mathrm{electrode}} = 1.04$ mm, $D_{\mathrm{bubble}} = 1.75$ mm.

homogeneous and spread out in the gas gap between the electrodes.

To compare emission intensity over the RVO region the total light emitted from the discharge for the sorted dataset is plotted as a function of time from the start of the voltage pulse (figure 10). The peak intensity occurred once the breakdown at the central node had occurred. The light decayed quickly ($\tau_{\mathrm{emission}} = 15$ ns) after the initial pulse but was observed to increase following the subsequent positive RVO peak of $V \approx 12$ kV. To account for the detected increase in light, the approximate power delivered to the plasma is plotted in figure 10 such that,

$$P_{\mathrm{plasma}} \approx V_{\mathrm{measured}} I_{\mathrm{plasma}}\ , \qquad (4)$$

where the plasma current is,

$$I_{\mathrm{plasma}} = I_{\mathrm{measured}} - I_{\mathrm{d}} - I_{\mathrm{f}} \qquad (5)$$

$$= I_{\mathrm{measured}} - C_{\mathrm{gap}} \frac{\mathrm{d}V_{\mathrm{measured}}}{\mathrm{d}t} - \frac{V_{\mathrm{measured}}}{R_{\mathrm{liquid}}}\ . \qquad (6)$$

The capacitance ($C_{\mathrm{gap}} \approx 3-6$ pF) used for the displacement current, I_{d}, was calculated across the diameter of the bubble ($D_{\mathrm{bubble}} \approx 1.5$ mm) as well as through the remaining liquid for the radius of the flat electrode. For the free current, I_{f}, the resistance of the surrounding liquid ($R_{\mathrm{liquid}} \approx 4\ \mathrm{k\Omega}$) was calculated from the radius of the electrode ($r_{\mathrm{electrode}}$) as a function of the conical electrode angle (see supplemental material

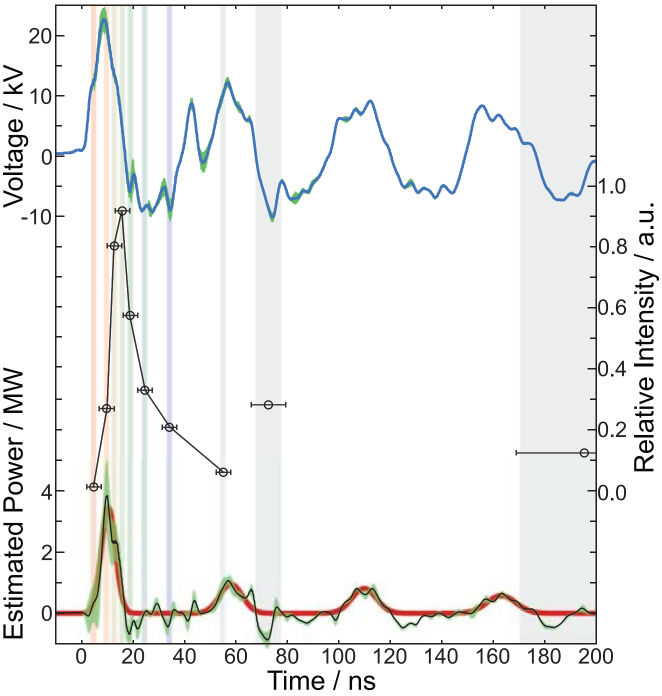

Figure 10. Comparison between voltage waveform, total emission intensity per image, and estimated power delivered to the plasma. Detected emission rapidly grows and then decays on the fall of the initial pulse, 6 ns after the peak of the power delivered to the plasma. Emissions detected in the RVO region have a measured signal greater than the initial detected emission. Physical parameters: $\sigma = 1.6$ mS cm^{-1}, $d_{\text{electrode}} = 1.04$ mm, $D_{\text{bubble}} = 1.75$ mm.

figure S5). It is important to note that the current measurement was limited by the usable rise time (5 ns) of the current monitor, which could not reliable resolve the ∼3 ns rise time of I_d. However, the conductivity of the water resulted in I_f contributing approximately half of I_{measured}, reducing the average rise time to ∼7 ns. A series of Gaussian functions were fitted to P_{plasma} in figure 10 to emphasize that the 5 ns temporal uncertainty of I_{measured} should be interpreted as a general guide for when an increase in emission was expected. The peak emission occurred ∼6 ns after the peak power. The images taken after the second and fourth oscillations overlapped with the delay and corresponded to the relative intensity expected during the periods of increased power. The peak-normalized emission intensity was 0.27 after the second power pulse and 0.13 after the fourth power pulse (figure 10). The corresponding peak-normalized values for the approximate plasma power were 0.30 for the second pulse and 0.16 for the fourth pulse. The agreement of these estimates suggests that power was delivered to the discharge well after the initial voltage pulse. This was consistent with the delayed discharges observed in DI water as detailed in our previous work and in other studies [30, 34]. However, several breakdown initiation locations were observed for subsequent pulses in DI water, whereas subsequent pulses expand the central emission node in the gas region of the bubble for the conductive liquid case presented in figure 9.

The experimental findings presented here indicate a strong dependence on the liquid conductivity for the initiation of breakdown within a bubble. For DI water, breakdown in a bubble was aided by the mechanism of cavitation-formed streamers in the liquid region before gas breakdown, unique to ns-pulsed discharges. In a conductive liquid, to achieve similar electrical conditions as DI water for the same applied voltage pulse, the bubble was perturbed by contact with the electrodes. Breakdown was achieved in preexisting bubbles in conductive solutions, but streamer formation was not observed.

4. Discussion

The importance of charge relaxation timescales is the fundamental motivation for the use of ns and sub-ns pulsed power supplies for conductive liquid applications. A comparison between the present experiments and other time-resolved imaging experiments for bubbles in conductive media are carried out in section 4.1 to discuss similarities and emphasize the significant differences that arise when attempting to capture breakdown evolution in bubbles. The phenomena of breakdown in bubbles, primarily focusing on the effects of charge neutralization due to the liquid medium around the bubble, are discussed in section 4.2. As conductivity is increased, charge 'leaks' into the bulk liquid and surface charges that generate surface ionization waves are reduced resulting in a diffuse breakdown in the central region of the bubble.

4.1. Breakdown in bubbles: experimental comparisons

To better understand the nanosecond breakdown dynamics, we utilized time-resolved imaging and focused on single-shot pulses to capture the progression of the breakdown over the lifetime of discharge events relative to a ns pulse. The present work has demonstrated that slight variations in bubble shape and position can alter the electrical characteristics of the measured voltage. Likewise, electrode shape and liquid properties have significant impact as well. Therefore, comparisons between systems should be made cautiously, keeping in mind that differences introduce variations in breakdown dynamics. Table 2 lists the experimental parameters for several studies including the present work [9, 24, 25, 30].

Hamdan *et al* experimented with positioning a gas bubble between a pointed pin and a hollow needle, which resulted in axial discharges within the bubble volume, as opposed to charges accumulating on the surface. They used two different time gates on an ICCD camera: 1 μs for the overall light emission of a single shot, and 2 ns to determine the lifetime of the plasma. For DI water, they observed a relatively symmetric discharge throughout the lifetime of the plasma. This can be compared to [30] for two pin electrodes demonstrating a periodic change of polarity of the electrodes over the lifetime of the decaying RVO. The exposure time of 1 μs made it impossible to resolve the breakdown process in Hamdan *et al*. Exposure times in the nanosecond range were needed to resolve the

Table 2. Comparison of experimental conditions between Hamdan *et al* [24], Lai and Foster [9, 25], and the present and previous works [30]. FWHM is the measured pulse width, $d_{\mathrm{electrode}}$ is the electrode gap distance, D_{bubble} is the unperturbed bubble diameter, σ is the conductivity of the liquid, and Δt_{gate} is the ICCD exposure gate width.

Experiment	FWHM (ns)	V_{peak} (kV)	$d_{\mathrm{electrode}}$ (mm)	D_{bubble} (mm)
Hamdan *et al*	10	15	1–2.5	1
Lai and Foster	120	20	30	3.5–4.5
Present work	10	22	1–2	1.7
	σ (μS cm^{-1})	Feed gas	Electrolyte	Δt_{gate} (ns)
Hamdan *et al*	10–1000	Ar	KCl	1000
Lai and Foster	0.1–13 000	Ar	KCl	5
Present work	1.5–11 000	Ar	NaCl	2

breakdown process, as seen in [9, 25, 30] and in this current work. Hamdan *et al* found that enhancing the conductivity of the water around an argon bubble resulted in decreased likelihood of discharge and less charge being injected into water of conductivity up to 1.0 mS cm^{-1} and the authors state discharge was unachievable beyond their upper conductivity limits. Distinct separation of the overall discharge into two faintly connected emission nodes was observed for increased conductivity. This agrees with the present observation that breakdown occurred near each electrode but does not result in a surface ionization wave across the bubble interface. In addition, resolving the temporal evolution of plasma depended on retaining reproducible boundary conditions from shot to shot and was thoroughly addressed in the current work.

Lai and Foster approached this issue by holding the bubble within a pseudo-two-dimensional framework, ensuring stable boundary conditions [9, 25]. Two quartz/plexiglass panels were constructed around the feed-gas nozzle and electrode such that a thin layer of gas (2D bubble) was discharged in a water film system up to 12.9 mS cm^{-1}. In their experiment the surface discharge dominated and the discharge around the edge of the bubble becomes brighter. Greater conductivity in the liquid allowed charges to spread rapidly, causing interfacial streamers to inhibit axial streamers over time. In liquids with reduced conductivity, the influence of surface charge became predominant, stopping the progression of streamers within the bubble. However, the surface of the quartz panel can also accumulate charge, introducing unintended effects not present in a natural 3D bubble. Compared to a submerged 3D bubble, where current can first flow directly between the electrodes and the liquid, the free current was initiated through plasma resistivity. This might explain their observation of the most intense emissions at $\sigma = 12.9$ mS cm^{-1}, a scenario not observed in Hamdan *et al* or the present experiment. In general, their findings were in agreement with nonPDPSIM models carried out by Babaeva and Kushner in which boundary-hugging streamers transitioned to axial streamers through the center of the bubble with increasing conductivity [28]. However, it is clear that the cases for a submerged bubble exhibited breakdown behavior different from bubbles confined by solid dielectric boundaries.

This work achieves reproducible boundary conditions for 3D free flowing bubbles by implementing an elaborate timing and sorting scheme which also adds a numerical qualification to reproducibility of bubble position and electrical characteristics (section 3.1). This enabled imaging with 2 ns exposure time resolution.

4.2. Charge dynamics and breakdown limitations

Here we reconstruct a detailed qualitative picture of the discharge process in conductive solutions with conductivity up to 1.6 mS cm^{-1}. Breakdown is expected when $\alpha d_{\mathrm{electrode}} = 1$ and streamer formation occurs when $\alpha d \approx 20$ under the Meek criterion, where α is the first Townsend coefficient. Under atmospheric conditions for argon, breakdown initiation is estimated by

$$\frac{\alpha}{p} = A\ exp\left[-\frac{Bp}{E}\right], \tag{7}$$

where $A = 12$ cm^{-1} Torr^{-1} and $B = 180$ V cm^{-1} Torr^{-1}, and $p = 760$ Torr [35]. The expected thresholds for a bubble in a $\sim$1 mm gap are $E \approx 2$ MV m^{-1} for breakdown and $E \approx 3.6$ MV m^{-1} for streamer formation. E-field in the gas region for the bubble dimensions in figures 4(a) and (b) exceeded conditions for the Meek criterion near the electrode. For the perturbed bubbles (figures 4(c) and (d)), E-field was within an order of magnitude of meeting the Meek criterion, but certainly exceeded breakdown conditions within the gas region. Therefore, based on a naive assessment, one might expect breakdown and streamer formation for all cases in figure 4. However, these estimates neglect the charge dynamics in the conductive liquid and the quenching effect of humid argon.

In addition to gas phase, the possibility of discharge in water in the electrode region was also explored. Calculations were carried out for the liquid region to evaluate the magnitude and direction of the current and deposition of energy. The total deposited energy density through Ohmic heating, u_{Ohm}, is given by the time integral over the modeled pulse duration,

$$u_{\mathrm{Ohm}} = \int_{t_{\mathrm{rise}}}^{t_{\mathrm{fall}}} \mathbf{E}\cdot\mathbf{J}\mathrm{d}t\,, \tag{8}$$

where $\mathbf{E}$ is the electric field vector and $\mathbf{J}$ is the current density vector in the liquid calculated by the electric transient solver in

Ansys Maxwell. In this experiment, Ohmic heating was calculated using equation (3) for the liquid region around the tip of the electrode. The results for varying liquid conductivity were,

$$u_{\text{Ohm, DI}} \approx (9.5 \pm 2.5) \times 10^4\ \text{J m}^{-3}$$
$$u_{\text{Ohm}},\, 1.6\,\text{mS cm}^{-1} \approx (8.5 \pm 2.5) \times 10^7\ \text{J m}^{-3}$$
$$u_{\text{Ohm}},\, 11\,\text{mS cm}^{-1} \approx (5.5 \pm 1.5) \times 10^8\ \text{J m}^{-3}\ .$$

Conventionally, for μs-pulsed or AC driven breakdown in conductive liquids, initiation occurs in the region of newly-formed vapor bubbles. These bubbles are created through Ohmic heating and can occur on timescales from a fraction to hundreds of microseconds depending on the magnitude or polarity of the applied voltage [22, 36]. Operation at ns timescales shorter than the expansion rate of liquid vaporization is essential to preclude the introduction of unintended bubbles and thermalization of the liquid. Vapor formation at the tip of the sharp electrode requires enough energy deposition via Ohmic heating per unit volume to result in either evaporation ($u_{\text{ev}} = 2.2 \times 10^9\ \text{J m}^{-3}$) or electrolysis ($u_{\text{el}} = 1.4 \times 10^9\ \text{J m}^{-3}$) [37]. The energy density calculated for Ohmic heating show that vaporization is not expected for the conductivity range of this experiment.

However, for DI water, figure 6 clearly showed that the most intense breakdown occurs between the tip of the electrode and apex of the bubble. When electric breakdown occurs directly at the electrode it can create a conducting channel that allows the plasma to propagate in the liquid region as well as the gas phase [30, 33, 34]. If a sharp electrode is excited to HVs so that the combination of a small electrode radius and a steep voltage rise generate sufficient electrostrictive pressure, nanoscopic cavitations (nanovoids) can form in the liquid phase allowing for electron acceleration to energy levels capable of ionizing water molecules in the vicinity [37–39]. The ratio of the E-field at the tip of the electrode and the E-field at the apex of the bubble increased linearly as the liquid thickness increases. If the bubble was too close to the electrode, the E-field in the gas region was simulated to be slightly higher. If the conditions were met to result in cavitation-initiated breakdown, the streamer channel propagating through the liquid acts as an extension of the electrode. This was investigated for DI water exclusively in our previous publication [30].

By comparison, increasing the conductivity of the bulk liquid reduced the amount of time that charge is allowed to accumulate on a surface before dissipating into the conductive bulk liquid as free charges. Though direct breakdown in conductive liquid has been observed experimentally ($V_{\text{peak}} >$ 80 kV at $\Delta t_{\text{rise}} \approx 2.5$ ns for a maximum liquid conductivity of 0.5 mS cm^{-1} [40]), the required voltage rate-of-rise exceeds achievable limits of the experiment presented here. If nanovoids cannot form through electrostrictive cavitation, then an electron-dense conductive channel cannot extend the E-field closer to the bubble. Energy appears to be deposited into the system, evidenced by the reduction in RVO when a sufficient layer of conductive liquid resides between the electrode and gas bubble (figure 5). The deposited energy was distributed through the volume of the liquid fast enough to inhibit any breakdown in the gas even when E-field strengths in the gas region exceed the breakdown threshold for Ar gas. For the high conductivity case of $\sigma = 11.0$ mS cm^{-1}, breakdown was not achieved, even for a reduced inter-electrode distance of $d_{\text{electrode}} = 0.74$ mm (see supplementary material figure S7).

The mobility of ions effectively neutralizes space charge in the dielectric and can be macroscopically quantified with the Maxwell relaxation time, derived from the continuity equation for free charge density,

$$\frac{\partial \rho_{\text{f}}}{\partial t} + \boldsymbol{\nabla}\cdot\mathbf{J}_{\text{f}} = 0 \tag{9}$$
$$\frac{\partial \rho_{\text{f}}}{\partial t} + \frac{\sigma}{\varepsilon}\rho_{\text{f}} = 0\ , \tag{10}$$

such that the solution is $\rho_{\text{f}}(t) = \rho_0 \exp[-t/\tau_{\text{M}}]$ and $\tau_{\text{M}} = \varepsilon/\sigma$. The Maxwell and Debye relaxation times are both related to the polarization behavior of dielectric materials, but they are based on different physical mechanisms. The Debye relaxation time, $\tau_{\text{D}} \approx 8$ ps, is related to the dipole moment reorientation of polar molecules in response to an external electric field. On the other hand, the Maxwell relaxation time is related to the time it takes for charges to redistribute in a dielectric material in response to an external electric field illustrated in figure 11. Under the conditions of this experiment, the Maxwell relaxation times were:

$$\tau_{\text{M, DI}} = 4.8\,\mu\text{s}$$
$$\tau_{\text{M}},\, 1.6\,\text{mS cm}^{-1} = 4.6\,\text{ns}$$
$$\tau_{\text{M}},\, 11\,\text{mS cm}^{-1} = 0.6\,\text{ns}\ .$$

On a microscopic scale, there is a residence timescale for ions to accelerate from their hydration shell within an electric field. The ion mobility, μ_{ion}, is inversely proportional to molecular radius, and thus, will respond on timescales of the hydration shell relaxation time (~10 s of ps for NaCl) [41]. Figure 11 illustrates the range of effects across timescales from polarization to the decay of the RVO.

For the case of DI water the charge accumulates at the boundary surface over time that is orders of magnitude longer than t_{rise} and t_{fall}, and even the decaying RVO will have dissipated before the time $\tau_{\text{M, DI}}$. Accumulated surface charges reside at the bubble boundary well beyond the lifetime of the applied voltage and these accumulated charges propagate as a surface ionization wave (timescale III in figure 11). This is evident for the propagation of the discharge in figure 6, which likely formed when charge on the bubble results in a surface ionization wave. In contrast, when τ_{M} is shorter than streamer initiation (timescale III in figure 11) charge leaks into the resistive liquid barrier and maintains a corona-like node instead of propagating as surface ionization wave across the bubble boundary.

The faint emission observed in figure 9(a) began the Townsend process by the time $\tau_{\text{M},1.6\,\text{mS cm}^{-1}}$, as illustrated in timescale II in figure 11. On this timescale breakdown occurs and expands in the volumetric gas region as the free charges in the plasma are neutralized at the surface boundary of the

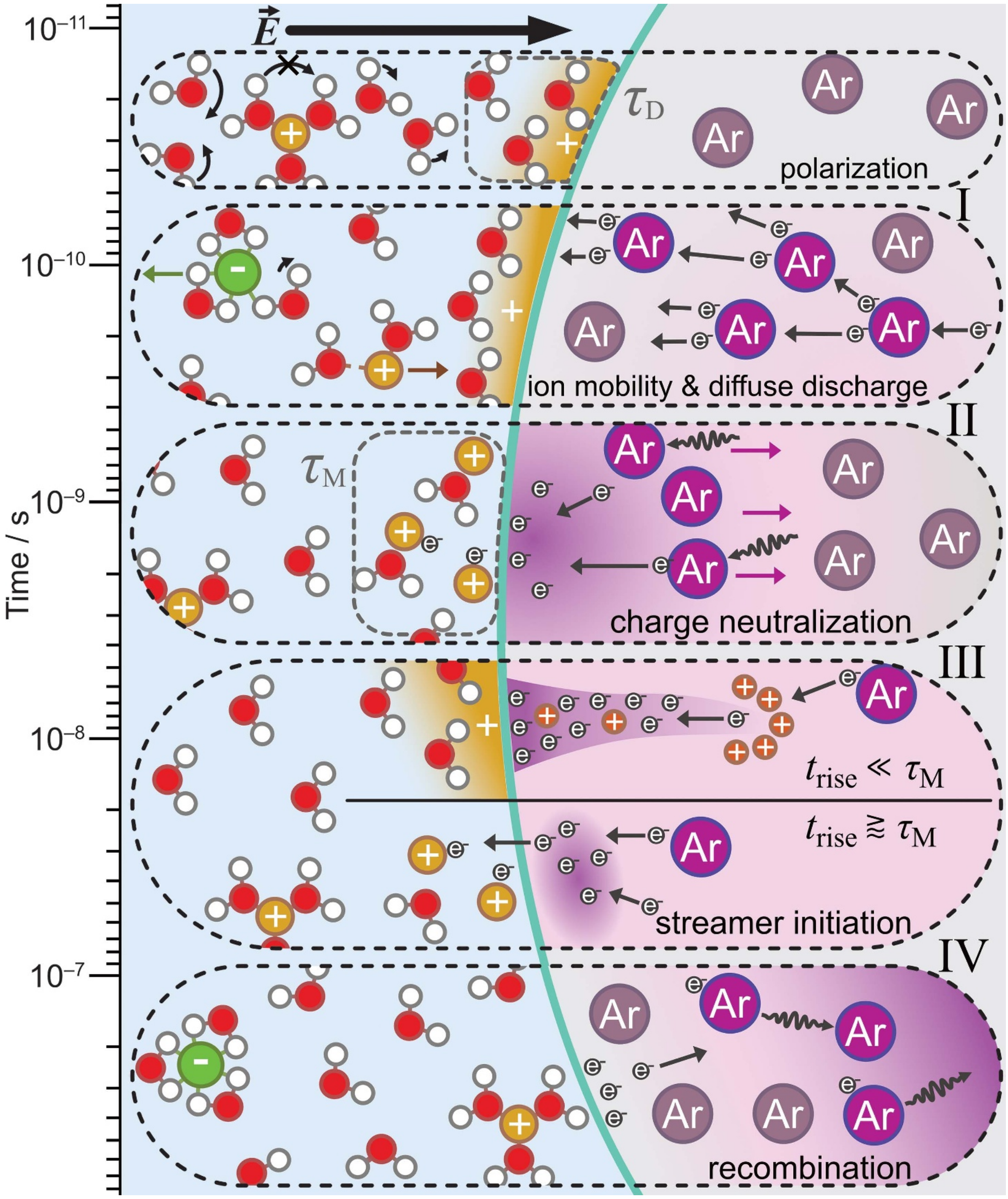

Figure 11. Timescale illustration of molecular and ionic reorientation and gas breakdown under an external electric field. Polarization of the water molecules and the bubble surface occurs around times of $\tau_D \approx 8$ ps. (I) Hydration shell residence times occur at 10–100 s of ps followed by initial Townsend avalanches. (II) Charge neutralizations occur on τ_M timescales and corona-like discharge is observed in ns. (III) Streamer initiation begins at > 10 ns. (IV) After the pulse ends emission from recombination is observed throughout the gas region.

bubble over the course of the initial pulse. This discharge residing in the gas volume of the bubble helps explain the increase of light at later pulses, despite having such small voltage peaks. If all of the discharge was bound to the surface of the gas/liquid interface, then it would be expected that enough of the charge would be neutralized by several $\tau_{M,1.6\,\mathrm{mS\,cm^{-1}}}$; but, the small increases in plasma power, and increased emission, at ~60 ns after the initial pulse suggests some plasma is sustained from collisions in the argon (figure 10).

When taking into consideration the breakdown properties at the interface of the material, it is important to note the effects conductivity has on the liquid permittivity. Babeva and Kushner simulated the effect that conductivity and permittivity have separately on plasma properties

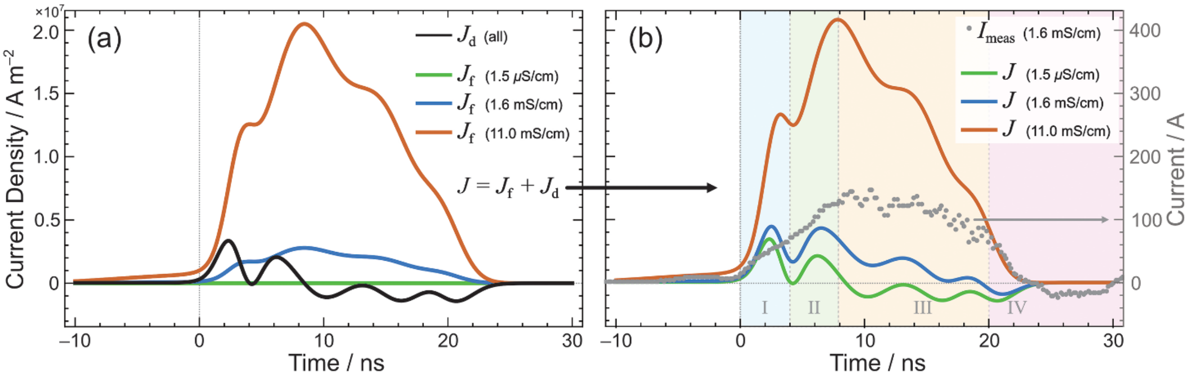

Figure 12. Calculated current densities for the applied voltage pulse for increasing conductivity. (a) The displacement current (black) varies negligibly between the varying conductivity, while the contribution from the free current in the liquid is substantial by comparison. The total current (b) for each conductivity is plotted alongside the current measured for the 1.6 mS cm^{-1} case. Temporal regimes are divided by images captured for this conductivity case into the (I) Townsend, (II) Initiation, (III) Streamer inhibition, and (IV) Decay regimes.

at the liquid/gas interface, but ion concentrations significantly impact both these quantities [28]. Wang and Anderko developed a model based on an empirical modification of the Kirkwood theory to calculate the reduction of ε_r of water for not only salt concentration, but specific ions of the salt [7]. Cations with a smaller radius make a greater contribution to the reduction of ε_r than those with a larger radius. When determining breakdown behavior in a given liquid, it is important to consider all these parameters. Ion mobility depends on the hydration shell residence time and the relaxation of shear stress between the molecules, simulated to occur on timescales of tens to hundreds of picoseconds [26, 42, 43].

In the case of $\tau_{\mathrm{M},11\,\mathrm{mS\,cm}^{-1}}$ the inability to achieve breakdown at extreme bubble/electrode contact and perturbation is attributed to the sub-ns timescale and alternatively insufficient applied voltage level and rise time. The response of the ions to neutralize surface charges occurs at timescales of 10 s–100 s of ps (timescale I in figure 11). This response is faster than the time observed to form the initial bright corona-like node in gas near the tip of the electrode. Charge and energy is transported around the bubble as the medium begins to approximate a resistor as opposed to a capacitor. The current associated with different charge transfer mechanisms operates on different time scales depending on whether the electric field is rotationally reorienting or translationally transporting charges. The value for E_{bubble} (equation (1)) is used to calculate and differentiate the free and displacement current,

$$\mathbf{J} = \mathbf{J}_\mathrm{f} + \mathbf{J}_\mathrm{d} \tag{11}$$

$$= \sigma\mathbf{E} + \boldsymbol{\nabla}\times\mathbf{M} + \frac{\partial\mathbf{P}}{\partial t} \tag{12}$$

$$\approx \sigma\mathbf{E} + \varepsilon_0\left(\varepsilon_\mathrm{r} - 1\right)\frac{\partial\mathbf{E}}{\partial t}\ , \tag{13}$$

where σ is the conductivity of the solution, the magnetization current ($\mathbf{J}_m = \boldsymbol{\nabla}\times\mathbf{M}$) is neglected, ε_0 is the permittivity of the vacuum, and the relative permittivity of water in the MHz range (corresponding to the rise and fall of the pulse and f_{RVO}) is $\varepsilon_\mathrm{r} \approx 78.36$ [44]. The E-field and current density was calculated and averaged at rings $\pm 2\ \mu$m around the 3D bubble surface (see supplementary material figure S4).

This is illustrated in figure 12, where individual components of the charge density are plotted using equations (1), (3), and (13). The black line in figure 12(a) is the average displacement current due to polarization. The change between the relative permittivity on this scale ($76 < \varepsilon_\mathrm{r} < 81$) results in a negligible change in J_d. The colored lines show the value for the free current carried by ions. Figure 12(b) shows the total current density for each case, $|\mathbf{J}|$, along with the average measured current for the sorted group used for imaging. The current is split into four regions of observed discharge (cf figures 7 and 8),

I Townsend regime: emission is extremely faint and homogeneous throughout the electrode gap,
II Initiation regime: initial emission point-source appears and EMI is detected on the current measurements,
III Streamer inhibition regime: emission begins and rapidly increases near the second electrode,
IV Decay regime: detected emission quickly decays and the spatial characteristic of the emission spreads from the middle node.

These regions are qualitatively associated with timescales in figure 11. Of course, the E-field does not peak instantaneously, so mechanisms faster than t_{rise} occur at different thresholds relative to the pulse shape.

It is clear from the plot that the polarization current is a significant portion of the total current for the cases in which breakdown occurs. The rate at which free charge is transported through the liquid in the 1.6 mS cm^{-1} case is still small for the faint Townsend regime. By the time the free current in this case dominates, the breakdown in the bubble has already begun and now the plasma resistance in the gas phase is likely reduced well below the liquid resistance, $R_{\mathrm{liquid}} \sim 4\,\mathrm{k}\Omega$. At this time, the plasma current density, $|\mathbf{J}_{\mathrm{plasma}}|$, acts as a dominant path for free charge. The calculated curve for the 11.0 mS cm^{-1} case confirms the negative result for electric breakdown. The free current in this case completely dominates within regime I, allowing for current pathways through the solution and neutralizing the space charges polarized at the bubble boundary interface. In previous work with a 1 μs pulse it was observed that the return current measured at the fall of the pulse for DI water was not present when conductivity was increased above 1 $\mathrm{mS\,cm^{-1}}$ [21]. This corresponded to an increasing current continuing over the lifetime of the pulse. This is in agreement with the present observation that charge accumulation at the bubble surface is attenuated and acts increasingly like a resistive element in the circuit.

This work contributes new insights into the behaviors of submerged bubbles under HV discharges, with emphasis on temporal resolution, breakdown occurrences, and emission patterns. Primary findings establish that the breakdown predominantly occurs near each electrode and does not result in an ionization wave that travels across the bubble interface. The importance of capturing the streamer formation on ns timescales between breakdown is demonstrated in this work. Multiple discharges over the decaying RVO from the applied voltage may appear as a single streamer if short enough exposure times are not used. Moreover, this work offers an explanation for differing discharge probabilities and intensities under varying conductivity, as well as divergent observations regarding the emergence of surface-hugging streamers across the bubble. The implications of these findings are substantial, offering a deeper understanding of the dynamic interactions between electric breakdown, submerged bubbles, and surrounding liquid medium. This study not only corroborates several observations from previous works, but also addresses discrepancies and extends the existing body of knowledge by increasing the imaging resolution of this phenomenon through the use of an experiment designed around the triggering of stable bubble dynamics.

5. Summary

This research aimed to deepen the understanding of plasma dynamics and its interaction within conductive solutions under nanosecond pulsed discharges. This understanding is key to optimizing the use of plasma in various applications and serves as a stepping stone for future research into the mechanisms of electric breakdown under these unique conditions.

The study included an investigation into the electrical response, breakdown, and propagation behavior in an argon bubble surrounded by a NaCl solution with varying conductivity. The approach was enabled by the synchronization of the applied voltage and diagnostic instruments accurately with the movement of the rising bubble. The experimental design effectively tackled the reproducibility challenges faced in prior studies by leveraging the stability of free-flowing bubbles to control the experiment's boundary conditions. Distinct differences in discharge initiation and development were observed for bubbles submerged in conductive water, compared to the ionization waves observed with the voltage pulse in this experiment for DI water. At higher conductivity, electric breakdown was only observed when the gas bubble came into direct contact with the electrode. No breakdown was observed in the liquid region, a significant departure from the behavior observed in deionized water under nanosecond pulses.

Breakdown stages for the images were divided into four regimes. The Townsend regime is characterized by the stage at which diffuse breakdown begins due to a sufficient E-field in the gas phase, prior to charge neutralization via Maxwell relaxation in the surrounding liquid. The Initiation regime is where a corona-like point near the electrode tip rapidly increases the measured current when the plasma current exceeds the polarization and liquid-free current. The Streamer inhibition regime occurs when, in DI water, a surface ionization wave would begin to propagate across the bubble. In a conductive solution, there is not sufficient time for charge to accumulate at the surface, and breakdown in the bulk gas dominates. Finally, in the Decay regime, after the pulse ends, the volumetric plasma expands quasi-isotropically, and particle recombination occurs for hundreds of nanoseconds.

In conclusion, this research significantly enhances the understanding of the interplay between plasma and conductive solutions, especially under nanosecond pulsed plasma conditions. The experiment focused on a pulse-width limited to the timescale of breakdown initiation. To further understand the behavior of plasma interactions with liquids, it is of interest to increase the applied voltage duration to include timescales that allow greater development of streamer formation and surface ionization waves. Exploring the time boundaries between the discharge regimes can aid in the understanding of the distinct mechanisms.

Data availability statement

All data that support the findings of this study are included within the article (and any supplementary files).

Acknowledgments

The work by N L S was supported by the Integrated University Program Graduate Fellowship. Work by K S was in part supported by the National Science Foundation under Grant No. PHY 2107901. All plasma imaging was conducted at the Princeton Collaborative Research Facility (PCRF) which is supported by U.S. DOE under the Contract No. DE-AC02-09CH11466. The work by S G was supported by PCRF.

ORCID iDs

Nicholas L Sponsel https://orcid.org/0000-0001-8172-9378
Sophia Gershman https://orcid.org/0000-0002-8409-4029
Katharina Stapelmann https://orcid.org/0000-0002-2116-2661

References

[1] Ranieri P, Sponsel N, Kizer J, Rojas-Pierce M, Hernández R, Gatiboni L, Grunden A and Stapelmann K 2021 *Plasma Process. Polym.* **18** 2000162

[2] Foster J E 2017 *Phys. Plasmas* **24** 055501

[3] Brandenburg R *et al* 2019 *Plasma Process. Polym.* **16** 1700238

[4] Myers B, Ranieri P, Smirnova T, Hewitt P, Peterson D, Quesada M H, Lenker E and Stapelmann K 2021 *J. Phys. D: Appl. Phys.* **54** 145202

[5] Vanraes P and Bogaerts A 2018 *Appl. Phys. Rev.* **5** 031103

[6] Vanraes P and Bogaerts A 2021 *J. Appl. Phys.* **129** 220901

[7] Wang P and Anderko A 2001 *Fluid Phase Equilib.* **186** 103–22

[8] Hamdan A, Profili J and Cha M S 2020 *Plasma Chem. Plasma Process.* **40** 169–85

[9] Lai J and Foster J E 2019 *J. Phys. D: Appl. Phys.* **53** 025206

[10] Shih K-Y and Locke B R 2009 *Plasma Process. Polym.* **6** 729–40

[11] Maehara T, Honda S, Inokuchi C, Kuramoto M, Mukasa S, Toyota H, Nomura S and Kawashima A 2011 *Plasma Sources Sci. Technol.* **20** 034016

[12] Shih K-Y and Locke B R 2011 *IEEE Trans. Plasma Sci.* **39** 883–92

[13] Wang H, Wandell R J, Tachibana K, Voráč J and Locke B R 2018 *J. Phys. D: Appl. Phys.* **52** 075201

[14] Tachibana K, Takekata Y, Mizumoto Y, Motomura H and Jinno M 2011 *Plasma Sources Sci. Technol.* **20** 034005

[15] Sommers B S, Foster J E, Babaeva N Y and Kushner M J 2011 *J. Phys. D: Appl. Phys.* **44** 082001

[16] Sommers B and Foster J 2014 *Plasma Sources Sci. Technol.* **23** 015020

[17] Gershman S and Belkind A 2010 *Eur. Phys. J.* D **60** 661–72

[18] Hamdan A and Cha M S 2015 *J. Phys. D: Appl. Phys.* **48** 405206

[19] Babaeva N Y, Naidis G V, Tereshonok D V and Smirnov B M 2017 *J. Phys. D: Appl. Phys.* **50** 364001

[20] Pillai N, Sponsel N L, Mast J, Kushner M J, Bolotnov I A and Stapelmann K 2022 *J. Phys. D: Appl. Phys.* **55** 475203

[21] Gershman S and Belkind A 2020 *J. Appl. Phys.* **128** 133302

[22] Panov V, Vasilyak L, Vetchinin S, Pecherkin V Y and Son E 2016 *J. Phys. D: Appl. Phys.* **49** 385202

[23] Panov V, Vasilyak L, Vetchinin S, Pecherkin V Y and Son E 2019 *Plasma Sources Sci. Technol.* **28** 085019

[24] Hamdan A, Čerņevičs K and Cha M S 2017 *J. Phys. D: Appl. Phys.* **50** 185207

[25] Ning W, Lai J, Kruszelnicki J, Foster J E, Dai D and Kushner M J 2021 *Plasma Sources Sci. Technol.* **30** 015005

[26] Lee S H and Rasaiah J C 1994 *J. Chem. Phys.* **101** 6964–74

[27] Rose D A and Benjamin I 1993 *J. Chem. Phys.* **98** 2283–90

[28] Babaeva N Y and Kushner M J 2009 *J. Phys. D: Appl. Phys.* **42** 132003

[29] Zhu T, Zhang Q, Jia Z and Yang L 2009 *IEEE Trans. Dielectr. Electr. Insul.* **16** 1552–7

[30] Sponsel N L, Gershman S, Herrera Quesada M J, Mast J T and Stapelmann K 2022 *J. Vac. Sci. Technol.* A **40** 063002

[31] Pillai N, Sponsel N L, Stapelmann K and Bolotnov I A 2022 *J. Fluids Eng.* **144** 021404

[32] Von Keudell A, Grosse K and Schulz-von der G V 2020 *Plasma Sources Sci. Technol.* **29** 085021

[33] Locke B R and Thagard S M 2012 *Plasma Chem. Plasma Process.* **32** 875–917

[34] Grosse K, Falke M and von Keudell A 2021 *J. Appl. Phys.* **129** 213302

[35] Raizer Y P and Allen J E 1991 *Gas Discharge Physics* vol 1 (Springer)

[36] Hogg M, Timoshkin I, Given M, Wilson M, MacGregor S, Wang T, Fouracre R and Lehr J 2012 *IEEE Trans. Dielectr. Electr. Insul.* **19** 1559–68

[37] Shneider M N and Pekker M 2019 *Liquid Dielectrics in an Inhomogeneous Pulsed Electric Field: Dynamics, Cavitation and Related Phenomena* (IOP Publishing)

[38] Seepersad Y, Pekker M, Shneider M N, Fridman A and Dobrynin D 2013 *J. Phys. D: Appl. Phys.* **46** 355201

[39] Grosse K, Held J, Kai M and Von Keudell A 2019 *Plasma Sources Sci. Technol.* **28** 085003

[40] Pongrác B, Šimek M, Ondáč P, Člupek M, Babický V and Lukeš P 2019 *Plasma Sources Sci. Technol.* **28** 02LT02

[41] Lee S H 2020 *Mol. Simul.* **46** 262–70

[42] Eiberweiser A and Buchner R 2012 *J. Mol. Liq.* **176** 52–59

[43] Samanta T and Matyushov D V 2020 *J. Chem. Phys.* **153** 044503

[44] Fernandez D P, Mulev Y, Goodwin A and Sengers J L 1995 *J. Phys. Chem. Ref. Data* **24** 33–70